Constraints on Climate and Habitability for Earth-like Exoplanets Determined from a General Circulation Model

Eric T. Wolf[1], Aomawa L. Shields[2,3,4,5], Ravi K. Kopparapu[5,6,7,8], Jacob Haqq-Misra[5,8], and Owen B. Toon[1]
[1] Laboratory for Atmospheric and Space Physics, Department of Atmospheric and Oceanic Sciences, University of Colorado, Boulder, CO, USA;
eric.wolf@colorado.edu
[2] University of California, Irvine, Department of Physics and Astronomy, 4129 Frederick Reines Hall, Irvine, CA 92697, USA
[3] University of California, Los Angeles, Department of Physics and Astronomy, Box 951547, Los Angeles, CA 90095, USA
[4] Harvard-Smithsonian Center for Astrophysics, 60 Garden Street, Cambridge, MA 02138, USA
[5] NASA Astrobiology Institute's Virtual Planetary Laboratory, P.O. Box 351580, Seattle, WA 98195, USA
[6] NASA Goddard Space Flight Center, 8800 Greenbelt Road, Greenbelt, MD 20771, USA
[7] Department of Astronomy, University of Maryland, College Park, MD 20742, USA
[8] Blue Marble Space Institute of Science, 1001 4th Avenue, Suite 3201, Seattle, WA, 98154, USA

Abstract

Conventional definitions of habitability require abundant liquid surface water to exist continuously over geologic timescales. Water in each of its thermodynamic phases interacts with solar and thermal radiation and is the cause for strong climatic feedbacks. Thus, assessments of the habitable zone require models to include a complete treatment of the hydrological cycle over geologic time. Here, we use the Community Atmosphere Model from the National Center for Atmospheric Research to study the evolution of climate for an Earth-like planet at constant CO_2, under a wide range of stellar fluxes from F-, G-, and K-dwarf main sequence stars. Around each star we find four stable climate states defined by mutually exclusive global mean surface temperatures (T_s); snowball ($T_s \leqslant 235\,K$), waterbelt ($235\,K \leqslant T_s \leqslant 250\,K$), temperate ($275\,K \leqslant T_s \leqslant 315\,K$), and moist greenhouse ($T_s \geqslant 330\,K$). Each is separated by abrupt climatic transitions. Waterbelt, temperate, and cooler moist greenhouse climates can maintain open-ocean against both sea ice albedo and hydrogen escape processes respectively, and thus constitute habitable worlds. We consider the warmest possible habitable planet as having $T_s \sim 355\,K$, at which point diffusion limited water-loss could remove an Earth ocean in $\sim$1 Gyr. Without long timescale regulation of non-condensable greenhouse species at Earth-like temperatures and pressures, such as CO_2, habitability can be maintained for an upper limit of $\sim$2.2, $\sim$2.4, and $\sim$4.7 Gyr around F-, G-, and K-dwarf stars respectively, due to main sequence brightening.

Key words: astrobiology – planets and satellites: atmospheres – planets and satellites: terrestrial planets

1. Introduction

Detecting Earth-like extrasolar planets is one of the primary objectives of ongoing and future exoplanetary observational surveys. Upcoming missions like the *James Webb Space Telescope* (Gardner et al. 2006), the *Transiting Exoplanet Survey Satellite* (Ricker et al. 2014), and others, will greatly improve our ability to detect and then begin characterizing terrestrial planets in the habitable zones of other stars. Still, observations will remain sparse compared to solar system objects and thus climate models are needed to interpret and understand these remote data. The conventional definition of the habitable zone requires liquid water to be extant and abundant at the surface continuously for at least several billion years in order for advanced life to evolve (Hart 1979). By definition, the fate of habitable worlds is inextricably tied to water and its associated feedbacks on the climate system. Thus, at its heart, the study of the habitable zone for Earth-like planets is the study of the fundamental evolutionary processes of water-rich terrestrial planetary atmospheres, touching upon end-member states that are characterized either by uncontrolled sea ice albedo or water vapor greenhouse feedbacks.

The sea ice albedo feedback can lead to rapid cooling whereupon the oceans become completely frozen over. Conversely, the water vapor greenhouse feedback can lead to abrupt warming, water-rich atmospheres, and the total of loss of the oceans due to hydrodynamic escape or a thermal runaway. For many years, the leading descriptions of long-timescale climatological evolution and the habitable zone have originated from energy balance and one-dimensional radiative–convective models (Budyko 1969; Hart 1979; Kasting et al. 1993; Selsis et al. 2007; Kopparapu et al. 2013). These works have shaped our thinking regarding the evolution of planetary climates. However, these models miss important feedbacks within the climate system caused by atmospheric dynamics, sea ice, clouds, and relative humidity.

Only recently have three-dimensional (3D) climate system models become commonly used to place limits on the habitable zone (Abe et al. 2011; Boschi et al. 2013; Leconte et al. 2013; Shields et al. 2013, 2014, 2016; Yang et al. 2013, 2014; Wolf & Toon 2014b, 2015; Godolt et al. 2015; Kopparapu et al. 2016; Popp et al. 2016). In both 3D and lower-dimensional models, the first objective has been to study an Earth-like planet, as Earth has the only climate system that is well observed and Earth is the only confirmed habitable world. As a first step, modern 3D climate systems models have been applied to study an Earth-like exoplanet as it evolves across the habitable zone due to changing stellar luminosity. 3D models allow for a self-consistent treatment of water in the climate system, including water vapor, clouds, surface ice, and oceans, and their respective spatial and temporal distributions about the planet. The presence or absence of each phase of water significantly affects the radiative energy budget of the planet, and thus the climate. However, there remains uncertainty

among different 3D Earth climate system models with regard to clouds (Flato et al. 2013), convection (Del Genio 2016), and radiative transfer (Yang et al. 2016). For instance, among leading climate models, the increase in global mean surface temperature of the Earth in response to a doubling of CO_2 varies between 2.1 and 4.7 K (Andrews et al. 2012). Differences can become more significant for exoplanetary problems where the implied forcings tend to be larger (e.g., see Figure 7(a) in Popp et al. 2016). We still have much to learn both scientifically and technically, as we apply our 3D models to the new and exotic atmospheres of extrasolar planets.

Here, we present simulations from a state-of-the-art 3D climate system model of an Earth-like planet with a fixed amount of CO_2 in its atmosphere around F-, G-, and early K-dwarf main sequence stars, over a wide range of stellar fluxes. We do not consider M-dwarf star systems in this study. Habitable zone planets around these low-mass stars are likely to be tidally locked, which has a profound impact on planetary climate (Yang et al. 2013, 2014; Leconte et al. 2015; Kopparapu et al. 2016; Way et al. 2016). Planets in the habitable zone of F-, G-, and early K-dwarf stars, as studied here, fall outside the tidal locking radius and thus can rotate rapidly, like we observe for Earth and Mars. Venus, however, falls outside the tidal locking radius but is a slow rotator due to atmospheric tides.

Here, we determine the climate of rapidly rotating terrestrial planets under varying stellar fluxes, and provide constraints on the habitable zone under fixed CO_2 conditions. The interaction of atmospheric circulation, water vapor, clouds, and surface ice all play critical roles in modulating climate, and controlling sharp positive feedbacks. While earlier studies have similarly mapped climate as a function of stellar insolation using energy balance or 1D models, to our knowledge this is the first such study to use an advanced, 3D climate system model to attempt to map the entire range of habitable climates, complete from snowball to moist greenhouse, around numerous types of main sequence stars.

2. Methods

Here, we use the Community Atmosphere Model version 4 (CAM4) from the National Center for Atmospheric Research (Neale et al. 2010). We build upon the prior work of Shields et al. (2013, 2014) and Wolf & Toon (2015) with new and complimentary simulations, facilitating a comprehensive description of the evolution of Earth-like climate through the habitable zones of F-, G-, and K-dwarf stars. Simulations of warm climates (i.e., those approaching a moist greenhouse) and cold climates (i.e., those approaching a snowball glaciation) follow the specific modeling methods described in detail in Wolf & Toon (2015) and Shields et al. (2013, 2014) respectively. Different setups for warm and cold simulations sets are used in order to combine new simulations with the prior simulations of Wolf & Toon (2015) and Shields et al. (2013, 2014), saving considerable computational expense. In total, we use data from ∼45 previous simulations from Shields et al. (2013, 2014) and Wolf & Toon (2015), and ∼45 new simulations, yielding a complete picture of habitable zone climates.

There are some differences in the specific configuration of CAM4 used for warm and cold simulations sets, including resolution, ocean heat transport, land area assumptions, and the radiative transfer module used in the calculation (see Table 1).

Table 1
Summary of "Cold" and "Warm" Model Configurations

Model Configurations	Cold[a]	Warm[b]
Moist physics	CAM4	CAM4
Horizontal resolution	$2° \times 2.5°$	$4° \times 5°$
Vertical levels	26	45
Model top (mb)	3	0.2
Radiative transfer[c]	Native	Correlated-k
Longwave range (μm)	5.0–1000	2.5–1000
Shortwave range (μm)	0.2–5.0	0.2–12.2
Continents	None	Present day Earth
Ocean heat transport	None	Present day Earth
Ocean albedo, visible/infrared	0.07/0.06	0.07/0.06
Sea ice albedo, visible/infrared	0.67/0.3	0.68/0.3
Snow albedo, visible/infrared	0.8/0.68	0.91/0.63
CO_2 (ppm)	400	367

Notes. Each uses the same core atmosphere model, with the same model physics, except where noted above.
[a] Used for simulations into and out of snowball states, see Shields et al. (2013).
[b] Used for simulations of moist greenhouse states, see Wolf & Toon (2015).
[c] See Yang et al. (2016) for a comparison of these two codes.

Of importance, cold simulations assume zero ocean heat transport and a global ocean, which allows for a transition to snowball Earth to occur at higher stellar fluxes than if some ocean heat transport is included (Poulsen et al. 2001; Pierre-humbert et al. 2011). Simulations approaching a moist greenhouse assume present day Earth continents and present day ocean heat transport. Cold simulations use the native CAM radiative transfer scheme found in CAM versions 4 and earlier (Ramanathan & Downey 1986; Briegleb 1992), while warm simulations use a correlated-k radiative transfer scheme (Wolf & Toon 2013). Both configurations use identical atmosphere, ocean, and sea ice physics (Neale et al. 2010). However, despite these noted differences, results from each configuration are well in agreement where simulations overlap, for conditions near present day Earth surface temperatures (see Section 3.1 and Figure 2).

All simulations assume an Earth-like planet, with Earth's mass and radius, a 50 m deep mixed-layer thermodynamic ("slab") ocean, and a 1 bar N_2 atmosphere with present day CO_2 concentrations but no ozone. Prognostic bulk microphysical parameterizations for condensation, precipitation, and evaporation control atmospheric water vapor, liquid cloud, and ice cloud condensate fields (Rasch & Kristjánsson 1998). Deep convection (i.e., moist penetrative) is treated using the parameterization of Zhang & McFarlane (1995). Shallow convective overturning is treated by the parameterization of Hack (1994). We use stellar spectra from F2V (σ Bootis HD 128167), G2V (the Sun), and K2V (ϵ Eridani HD 22049 and synthetic) stars (Pickles 1998; Segura et al. 2003). In Figure 1, we show F-, G-, and K- dwarf spectra normalized to 1360 W m^{-2}. These stars have effective temperatures (T_{eff}) of 6954, 5778, and 5084 K. In general F-, G-, and K-dwarf stellar classifications span 6000 K $\leqslant T_{\mathrm{eff}} \leqslant$ 7500 K, 5200 $\leqslant T_{\mathrm{eff}} \leqslant$ 6000 K, and 3700 $\leqslant T_{\mathrm{eff}} \leqslant$ 5200 K respectively (Habets & Heintze 1981). We do not consider photochemistry here, however the stellar type, stellar activity, and atmospheric oxygen concentration are all critical for determining the UV radiation hazard for the planet surface, and have been studied elsewhere (Segura et al. 2003; Rugheimer et al. 2015). For each planet, we assume Earth-like orbital characteristics, with an orbital
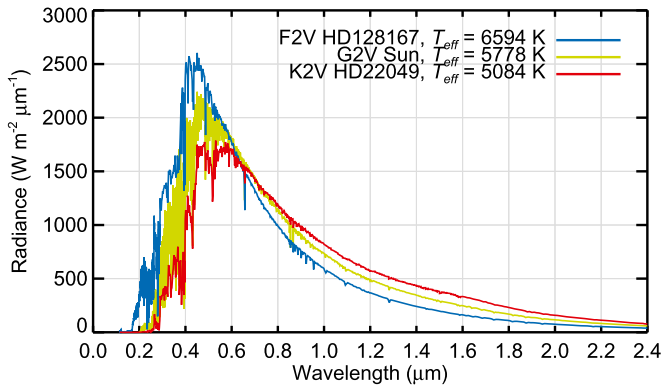
Figure 1. Empirical stellar spectra for F-, G-, and K-dwarf stars used in this study, normalized to a total flux of 1360 W m^{-2}.

period of 1 Earth year, zero eccentricity, and 23.5° obliquity. Differences in the semimajor axis and orbital period that arise due to the respective mass and luminosity of each star are not incorporated. However, changes to the orbital periods do not appreciably affect global mean climate for rapidly rotating planets within the habitable zones of F-, G-, and early K-dwarf stars (Godolt et al. 2015). For this study we assumed a 24 hr rotation rate for all simulations. This is reasonable, as habitable zones studied here are outside the tidal spin-down region of their respective host stars (Leconte et al. 2015).

3. Results

3.1. Control Simulations

First, we compare a set of standard atmospheres around F-, G-, and K-dwarf stars, using the model default present day Earth solar insolation of 1361.27 W m^{-2} (Table 2). In these simulations we assume the warm model configuration (Table 1), with a continental configuration and implied ocean heat transport that matches the present day Earth. The spectra emitted from cooler stars are relatively redder (Figure 1), and thus interact more strongly with atmospheric clouds, CO_2 and water vapor, as well as surface water ice and snow. Surface water ice (Dunkle & Bevans 1956), as well as atmospheric clouds, CO_2 and water vapor (Kasting et al. 1993; Selsis et al. 2007) strongly absorb in the near-infrared. The end result is that the spectrally averaged all-sky planetary albedo is lower for an Earth-like planet around cooler stars (Table 2). Thus it takes less stellar flux to warm an Earth-like planet around cooler stars. This albedo change is well established from simpler models and our results concur (Kasting et al. 1993; Kopparapu et al. 2013; Yang et al. 2014). The clear-sky (i.e., without clouds) albedo is reduced by a factor of ~2 between F- and K-dwarf control cases, owing to decreased Rayleigh scattering and increased overlap of the incident stellar spectra with near-infrared water vapor absorption bands. Meanwhile, the change in cloud albedo is relatively small across each different stellar type, varying by only about ~6% (analogously a cloud albedo change of ~0.01).

Nonetheless, in each control simulation the overall climate is not radically changed due to altering only the stellar spectra but not the stellar energy input (Table 2). Climate does not switch states, remaining (generally) like the present-day Earth, dominated by open ocean but with some sea ice at the poles. The strength of the greenhouse effect and the global mean cloud fraction remains fairly similar for each control case. Note

Table 2
Global and Annual Mean Quantities from Control Simulations Using the Warm Configuration, which Includes Ocean Heat Transport Identical to the Modern Earth

Star (type)	F	G	K
Surface Temperature (K)	281.4	289.1	294.8
2 m Air Temperature (K)	280.1	288.0	294.1
Albedo, All-sky	0.387	0.329	0.284
Albedo, Clear-sky	0.216	0.152	0.119
Albedo, Cloud	0.171	0.176	0.166
Albedo, Surface	0.143	0.114	0.104
Albedo, Rayleigh	0.073	0.038	0.015
Greenhouse Effect, Total (K)	35.3	37.6	39.5
Greenhouse Effect, Clear-sky (K)	25.0	28.5	31.3
Greenhouse Effect, Cloud (K)	10.3	9.1	8.2
Water Vapor Column (kg m^{-2})	15.7	26.5	41.2
Cloud Water Column (kg m^{-2})	0.093	0.115	0.129
Cloud Ice Column (kg m^{-2})	0.018	0.015	0.013
Cloud Fraction, Total (%)	69.5	66.3	64.3
Cloud Fraction, Low (%)	35.7	34.8	37.7
Cloud Fraction, Middle (%)	29.9	27.0	23.3
Cloud Fraction, High (%)	49.6	47.2	43.4
Sea Ice Fraction Relative to Ocean (%)	16.1	7.5	3.7
Snow Depth (m)	0.081	0.042	0.021

the greenhouse effect is given in units of temperature in order to facilitate comparison with Godolt et al. (2015), and is calculated using the Stefan–Boltzmann law from the difference in upwelling longwave radiation between the surface and the top-of-the-atmosphere implied by clouds and absorbing gases respectively. Differences in water vapor, cloud water, and sea ice fractions come as no surprise, as these quantities are strongly dependent on the planetary temperature. Differences in the evolution of sea ice, convection, clouds, and the distribution of relative humidity are significant drivers of planetary climate, and serve to amplify initial radiative perturbations due to albedo changes that are implied by changing the spectral energy distribution. For the F-dwarf star, cooling caused initially by increased atmospheric scattering and surface reflectivity is then amplified by the sea ice albedo feedback. For the K-dwarf star, warming caused initially by increased absorption by water vapor and the surface is then amplified by the water vapor greenhouse, and is also linked to cloud feedbacks.

Interestingly, our results shown in Table 2 exhibit remarkably less sensitivity to changes in the stellar spectra compared to a similar set of simulations conducted with the 5th version of the European Center Hamburg GCM (ECHAM5) from Godolt et al. (2015). Irradiated by the same F- and K-dwarf spectra, global mean surface 2 m air temperatures reach 280.1 K and 294.1 K in CAM4, while in ECHAM5 they reach 273.6 K and 334.9 K respectively. Note that Popp et al. (2016) similarly find that ECHAM is significantly more sensitive than CAM4 to increasing stellar flux from the Sun. The striking differences in climate between these simulations highlight the need for detailed model intercomparison to ascertain why the models diverge. Without further work, we cannot determine if the model differences arise purely from differences in radiative transfer, or whether sea ice and cloud feedbacks are more to blame.

For simulations near the present day surface temperatures, model configurations for warm and cold simulations (see
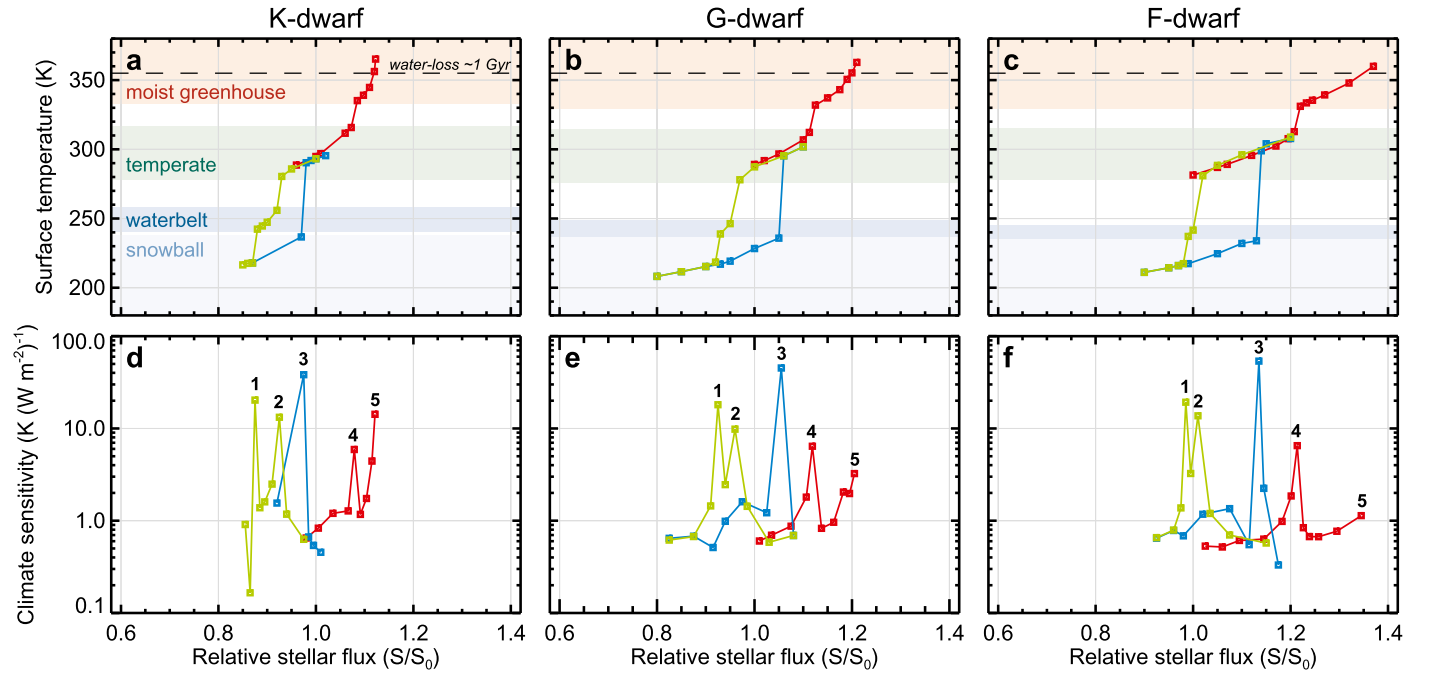
Figure 2. The evolution of global mean surface temperatures (panels a–c) and climate sensitivity (panels d–f) for Earth-like planets around F-, G-, and K-dwarf main sequence stars as a function of relative stellar flux (S/S_0). The four stable climate regions are labeled and indicated by shaded regions in the top panels. Different color lines are associated with different simulation sets. Red lines indicate simulations starting from modern Earth conditions, under a positive solar forcing (i.e., warming). Green lines indicate simulations starting from modern Earth conditions, under a negative solar forcing (i.e., cooling). Finally, blue lines indicate simulations starting from a globally glaciated state, under a positive solar forcing. Numbers in the bottom panels mark peaks in climate sensitivity and thus represent specific climatic transitions: (1) from waterbelt to snowball, (2) from temperate to waterbelt, (3) from snowball to temperate, (4) temperate to moist greenhouse, and (5) toward a runaway greenhouse. The black dashed line marks the climate where diffusion-limited water loss could remove an Earth ocean of water within about 1 Gyr.

Table 1) yield very similar results, with mean surface temperatures generally within ~2 K for temperate conditions (see Figure 2). Under the present day stellar flux from the Sun, a G-dwarf star, the cold (warm) configurations yield a global mean surface temperature of 287.3 K (289.1 K). Under insolation from an F-dwarf star, a 5% increase in the solar constant above the present day is required to reach approximately modern day surface temperatures of 288.4 K (287.1 K) for the cold (warm) configuration. For the K-dwarf star case, a 2% reduction in the solar constant yields 290.3 K (291.6 K) for the cold (warm) configurations. However, at colder temperatures, differences emerge between the warm and cold configurations due primarily to ocean heat transport, which is assumed not to occur in the cold configuration. At the present day solar flux, F-dwarf simulations become cold (241.6 K) when no ocean heat transport is included. This behavior in response to turning off ocean heat transport is in agreement with Godolt et al. (2015).

3.2. Multiple Climate States

Figure 2 shows the evolution of global mean surface temperature (T_s) and climate sensitivity for an Earth-like planet with fixed CO_2 as a function of the relative stellar flux from F-, G-, and K-dwarf stars. Relative stellar flux is defined as the ratio between the incident stellar flux on the planet, and that received by Earth at present day (S_0), taken here to be 1360 W m^{-2}. Thus, in Figure 2 a relative stellar flux (S/S_0) of 1.0 equals an incident stellar flux on the planet of 1360 W m^{-2}, approximately matching the present day Earth value of 1361 W m^{-2}. Four stable climatic regimes are indicated by shaded regions in Figure 2: snowball ($T_s \leqslant 235$ K), waterbelt (235 K $\leqslant T_s \leqslant 250$ K), temperate (275 K $\leqslant T_s \leqslant 315$ K) and

moist greenhouse ($T_s \geqslant 330$ K). Stable climates are in equilibrium, having balanced incoming and outgoing radiation and no systematic temperature drift. The evolution of climate around each type of star is qualitatively similar. Note that here we consider the moist greenhouse climate state to be defined by the radiative–convective state of the atmosphere, as described by Wolf & Toon (2015). Wolf & Toon (2015) found that the climate undergoes an abrupt transition between temperate and moist greenhouse states, characterized by the closing of the 8–12 μm water vapor window region, increased solar absorption in the near-infrared water vapor bands, and the subsequent stabilization of the low atmosphere against convection. We discuss water loss rates versus the depletion of the ocean inventory separately below. Under a relaxed constraint, where any amount of surface water may constitute a habitable planet, waterbelt, temperate, and cooler moist greenhouse states are habitable. However, in our surveys of the stars we seek not just to find habitable zone planets, but to find those that are preferably within the temperate climate regime, where the vast majority of the planet is ice-free and temperatures are similar to the Earth presently.

The four stable climate regimes are separated by sharp climatic transitions, indicated by maxima in climate sensitivity (numbered in Figures 2(d)–(f)). Climate sensitivity is the change in global mean surface temperature for a given change in radiative forcing, here from incrementally increasing or decreasing the incident stellar flux. The sharp climatic transitions are triggered by interactions between sea ice, water vapor, clouds, and radiation, whereupon a small change in solar forcing can beget a large change in T_s. Interestingly, for some temperature ranges, 250 K $\leqslant T_s \leqslant 275$ K and 315 K $\leqslant T_s \leqslant 330$ K, stable climate states never occur in our model. These unallowable temperature

regions are caused by uncontrolled sea ice albedo, and uncontrolled water vapor greenhouse feedbacks, respectively. Each cause climate sensitivity to spike (Figure 2). If $250\,K \leqslant T_s \leqslant 275\,K$, climatic stability can only be re-established either by warming into the temperate state where sea ice is trapped at the poles, or by cooling into the waterbelt state which is stabilized by albedo contrasts between bare sea ice and snow covered areas formed when global ice sheets encroach into the subtropical desert zone (e.g., Abbot et al. 2011). If $315\,K \leqslant T_s \leqslant 330\,K$, climate stability can only be re-established either by cooling into the temperate state where the planet's surface can efficiently cool to space through the water vapor window region, or by warming into the moist greenhouse state which is stabilized by a reduction to relative humidity and the formation of an upper atmosphere cloud deck (Wolf & Toon 2015). While these unallowable regions appear similarly for an Earth-like planet around each star, it is unclear how sensitive these regions may be to other choices of model parameters.

Earth presently exists in a region where two climate states are possible. In Earth's present temperate state (perhaps fortuitously) climate sensitivity is near a minimum against both positive and negative radiative forcings (Figure 2(e)). The relative long-term stability of Earth's climate may be circumstantial evidence that terrestrial climates preferentially relax toward climate sensitivity minima. As shown in Figure 2 and Shields et al. (2014), there is strong hysteresis between the snowball and temperate climate states, which has long been recognized from simple climate models (Budyko 1969). The solar constant must be raised to high levels to escape from a snowball, but at much lower solar constants temperate climate states are stable, but only if the climate was initially warm. Thus there is a range of stellar fluxes at which climate exhibits bistability, with both snowball or temperate and waterbelt states being possibly stable at given stellar fluxes. The actual state depends on the initial conditions, and thus the planet's evolutionary history. For planets around F-, G-, and K-dwarf stars, Earth-like planets exhibit bistability for relative stellar fluxes (S/S_0) of 0.99–1.14, 0.92–1.06, and 0.88–0.98 respectively. Note that the extent of the bistable region is encouragingly quite similar to that found from 3D models of intermediate complexity (Lucarini et al. 2010; Boschi et al. 2013), which found a bistable range of 0.93–1.05 for Earth around the Sun. Bistability is not found in our calculations between temperate and the moist greenhouse climate states. However, Popp et al. (2016) find evidence of a small (i.e., contained in a ~2% change in stellar flux) hysteresis between temperate and moist greenhouse climates using an idealized version of the ECHAM6 climate model.

The runaway greenhouse provides the most generous bounds for the inner edge of the habitable zone for an Earth-like planet. Kasting et al. (1993) also defined the more conservative "moist greenhouse" inner edge of the habitable zone based on water loss to space from moist atmospheres, which may occur at lower stellar fluxes than are needed to induce a thermal runaway. Kasting et al. (1993) define this inner edge constraint to occur where diffusion limited escape causes the entirety of Earth's oceans ($1.4 \times 10^{24}\,g\,H_2O$) to be lost to space in a period of time that approaches the present age of the Earth. In practical terms, this threshold is reached when the stratospheric H_2O volume mixing ratio equals 3×10^{-3}. Here we adopt a marginally more stringent constraint, assuming that an Earth

ocean of water must be lost within ~1 Gyr. This ensures that the water loss timescale is meaningful even for F-dwarf stars, which live little more than half as long as our Sun (Rushby et al. 2013). This escape rate occurs when the stratospheric water vapor volume mixing ratio exceeds $\sim 7 \times 10^{-3}$, which occurs in our model when $T_s \sim 355\,K$ around each star (Figure 2). However, note that Earth-like planets with $T_s \sim 350\,K$ will desiccate within about ~8 Gyr, which is near the main sequence lifetime of G-dwarf stars and significantly less than that of K-dwarf stars.

Figure 3 shows the model top (~0.2 mb) temperature and water vapor mixing ratio as a function of mean surface temperature, as climate warms around each star. The temperature controls the amount of water vapor in the upper atmosphere. At low T_s, the upper atmosphere is noticeably warmer around redder stars due to the effect of increased absorption by water vapor in the near-infrared, coupled with inefficient radiative cooling aloft. However, this trend becomes muted for increasing T_s as the atmospheres become increasingly water rich, thermally opaque, and convective to high altitudes (Wolf & Toon 2015). The timescale to lose Earth's oceans falls off dramatically as the mean surface temperature increases. By the time $T_s \sim 360\,K$, the oceans would be lost in only several hundred million years. Such atmospheres would be short-lived relative to stellar lifetimes, and would transition into dry planets (Abe et al. 2011). However, relatively cooler moist greenhouse atmospheres, with $330\,K \leqslant T_s \leqslant 350$, have upper atmosphere water vapor volume mixing ratios between $\sim 10^{-6}$ and 10^{-3}, and thus can retain an Earth ocean of water for tens to hundreds of billion of years. More detailed hydrodynamic escape calculations from these atmospheres would better our understanding of habitable lifetimes of planets near the inner edge of the habitable zone. Furthermore, on other planets, hydrogen escape rates may vary due to factors we have not considered, such as differences in the exobase temperature, the mean molecular weight of the atmosphere, the gravitational force, stellar activity, and photochemistry.

3.3. Circumstellar Climate Zones

Based on the climate results shown in Figure 2, we can define circumstellar climate zones for Earth-like planets at modern-day CO_2 levels around F-, G-, and K-dwarf stars (Figure 4). Here, circumstellar climate zones provide a more detailed description of habitable planetary climates than does the habitable zone. The habitable zone is based on the existence of liquid water, but does not take into account such issues as the ability of organisms to survive at a given temperature, or the climatological history of the planet. Significant differences in climate zones exist depending upon whether one assumes warm (i.e., ocean covered, Figure 4(a)) or cold (i.e., completely ice covered, Figure 4(b)) initial conditions. Following the practice of some recent habitable zone studies (Selsis et al. 2007; Kopparapu et al. 2013, 2014; Zsom et al. 2013; Yang et al. 2014), based on our climate modeling results we determine parametric relationships between the relative incident stellar flux received by an Earth-like planet at modern CO_2 that yields a given climate state ($S_{climate}$) noted in Figure 4, and the stellar effective temperature (T_{eff}) of the host star. Equations (1) and (2) are valid for stars with T_{eff} between 4900 and 6600 K

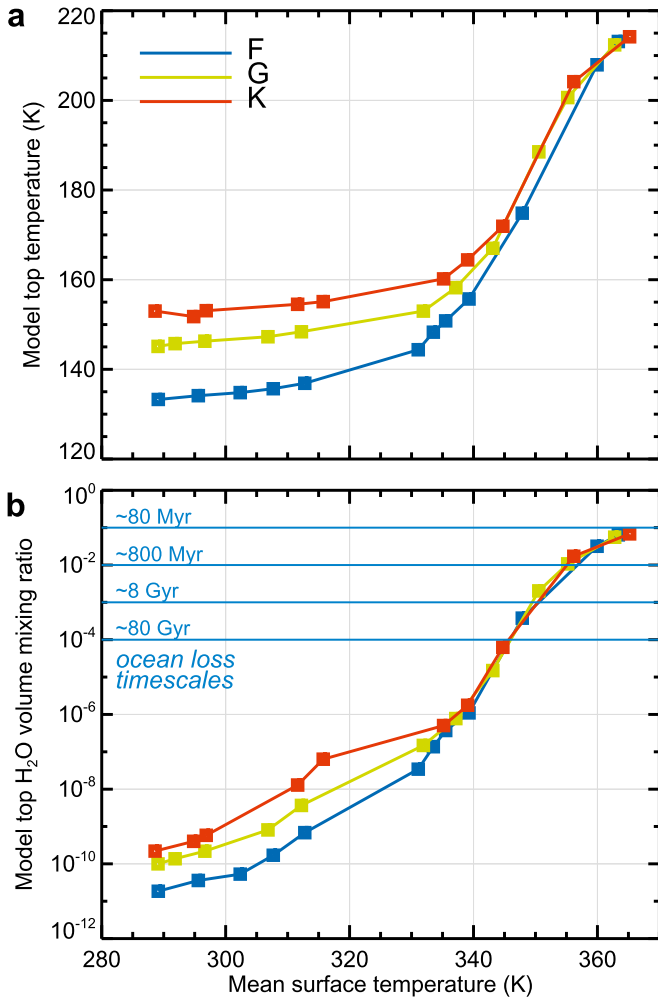$$S_{climate} = a + bT_* + cT_*^2 \qquad (1)$$

Figure 3. The model top temperature (a) and the model top water vapor volume mixing ratio as a function of mean surface temperature for planets around F-, G-, and K-dwarf stars. Note the model top pressure is ~0.2 mb. Ocean loss timescales are calculated as the time for diffusion limited escape to remove an Earth ocean of water from the planet.

$$T_* = T_{eff} - 5780 \text{ K}, \qquad (2)$$

where coefficients a, b, and c, are given in Table 3 for each particular climate. The results of $S_{climate}$ using Table 3 describe circumclimate zones that are plotted and labeled in Figure 4.

All circumstellar climate zones found in Figure 2 are shown in Figure 4 as shaded regions bounded by solid lines. Additional climate states of interest are indicated by dashed lines. First, moving from left to right in Figure 4(a) (from high T_s and high solar flux), we delineate with a dashed line the inner edge of the habitable zone according to the ~1 Gyr water loss criteria ($T_s \sim 355$ K) discussed in Section 3.1. Next we mark with a solid orange line the radiative–convective transition between a moist greenhouse climate state and a temperate state, as described by Wolf & Toon (2015), whereupon T_s abruptly changes between ~330 K and ~315 K. Next we mark the heat stress limit for mammalian biological functioning. Sherwood & Huber (2010) argue that if $T_s \geqslant 300$ K, then the majority of the Earth's human population would be subject to prolonged periods of lethal heat stress. While technological and biological adaptation may facilitate survival at these hotter temperatures, life and society as we know them would be threatened. Next, we mark the climatic conditions of the present day Earth

($T_s \sim 289$ K) around each star. In Figure 4(a) we define with a solid dark blue line the boundary where an Earth-analog planet with identical CO_2 would transition from the temperate regime into a waterbelt (i.e., ice lines reaching the tropics), a condition only accessible via cooling from a warmer state. Finally, we define with a solid light blue line the transition into a snowball Earth state via reduced stellar forcing. If formed initially warm, a planet may access a temperate zone with $\Delta S/S_0 \sim 0.16$–0.20 (equivalently a ~218–272 W m^{-2} change in total stellar insolation received by the planet) as marked by the green shaded region in Figure 4(a). Here, $\Delta S/S_0$ is the width of the climate zone in units of relative stellar flux and varies for planets around different effective temperature stars. The habitable zone, including the waterbelt state (for warm start only) up to the water loss threshold, spans $\Delta S/S_0 \sim 0.24$–0.34 (~326–462 W m^{-2}) for initially warm planets.

In the absence of CO_2 changes, if a planet is initially cold (i.e., fully ice covered), its habitable zone is constrained by the stellar driven deglaciation and water loss limits indicated in Figure 4(b), and there is a relatively small range of possible habitable states. Note that a present day Earth-like climate cannot be accessed from a cold start (Figure 4(b), see also Figure 2). Moving from right to left (from low T_s and low stellar flux), stellar driven deglaciation is indicated by a light blue line in Figure 4(b). The temperate climate zone is significantly narrower with 290 K $\leqslant T_s \leqslant$ 315 K, and the waterbelt state is skipped entirely from a cold start. There is no difference between the inner edge of the habitable zone for cold and warm start cases. By the time that the climate has warmed to moist greenhouse and water loss thresholds, snow and ice have long since vanished from the planet, and no memory of the cold initial conditions remain. Thus, the temperate climate regime spans only $\Delta S/S_0 \sim 0.06$–0.11 (~82–150 W m^{-2}) as marked by the green shaded region in Figure 4(b). The full width of the habitable zone for initially cold planets is marked from stellar driven deglaciation to water loss limits, and spans $\Delta S/S_0 \sim 0.14$–0.19 (~190–258 W m^{-2}). It is interesting to note that the habitable zone is wider for a cold initial planet around a K-dwarf star. This is because stellar driven deglaciation is more effective around relatively redder stars, due to the low near-infrared albedo of snow and ice (Joshi & Haberle 2012; Shields et al. 2014).

3.4. Habitable Lifetimes

Another consideration in Figures 2 and 4 is the time that is spent in the habitable zone. Main sequence stars brighten over the course of their lifetime, thus the radiation received by an orbiting planet increases over time (Iben 1967). However, the main sequence lifetime and rate of luminosity evolution depends upon the stellar type. If we assume that the rate of luminosity evolution is linear in time, we can then make simple estimates for the lifetime of climate zones ($\tau_{climate}$), calculated as the time needed for the stellar luminosity to evolve corresponding to the maximum width of each climate zone in terms of the relative stellar flux ($\Delta S/S_0$) shown in Figure 4. We use Equation (3):

$$\tau_{climate} = \frac{\Delta S/S_0}{\frac{L_{tms}}{L_0} - \frac{L_{zams}}{L_0}} \times \tau_{ms} \qquad (3)$$

where L_{tms}/L_0 is the luminosity at the end of the star's main sequence lifetime normalized to the present solar luminosity,
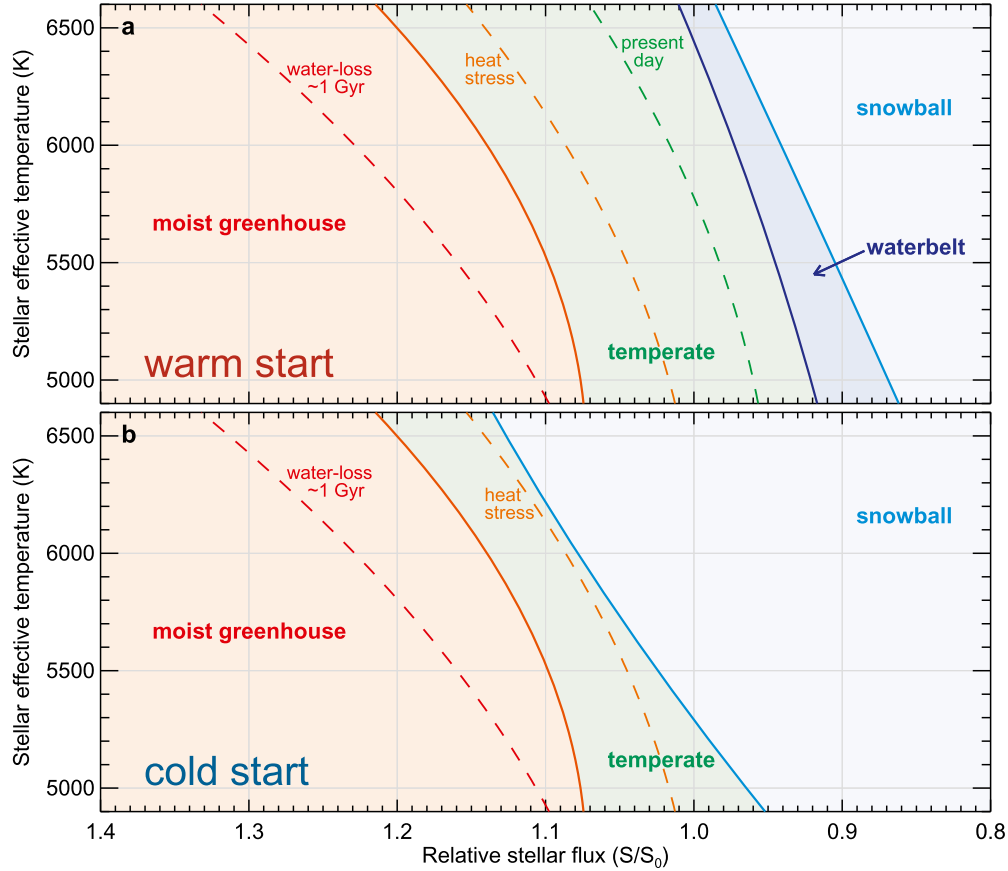
Figure 4. Circumstellar climate zones as a function of relative stellar flux for Earth-like planets at constant CO_2. The top panel assumes an initial state that is warm (i.e., liquid water covers the surface). The bottom panel assumes an initial state of a completely ice-covered planet.

L_{zams}/L_0 is the zero age main sequence luminosity normalized to the present solar luminosity, and τ_{ms} is the total main sequence lifetime of the star. L_{tms}/L_0 and L_{zams}/L_0 are calculated using the parametric fits given by Equations (3) and (5) in Guo et al. (2009). Following Rushby et al. (2013, Equations (7) and (8)), the total main sequence lifetime can be computed as:

$$\tau_{ms} = 10.9 * \frac{M_0}{M^3} \qquad (4)$$

where M is the mass of the star, M_0 is the mass of the Sun, and 10.9 is the main sequence lifetime of our Sun in billions of years. Our calculation of $\tau_{climate}$ assumes that the planet initially has the lowest temperature allowed for a given climate zone, and is then warmed via main sequence brightening through the climate zone. Thus $\tau_{climate}$ is the maximum length of time that an Earth-like planet, at fixed CO_2, could remain within a given climate zone under the influence of the main sequence brightening. Beginning its life at a higher temperature would decrease $\tau_{climate}$, while a draw down of CO_2 could possibly lengthen $\tau_{climate}$.

In Figure 5 we consider $\tau_{climate}$ for the temperate climate zone, and for the habitable zone in total, including waterbelt and moist greenhouse states with T_s below 355 K. Viewed in this fashion, it is clear that lower effective temperature stars (i.e., the K-dwarf) provide a more stable climatic environment because $\tau_{climate}$ for K-dwarfs is about double that of the F- and

G-dwarf stars. While habitable planets around K-dwarf stars are generally more sensitive to changes in the stellar flux than planets around F- and G-dwarfs (Figures 2(a), (d)), their long main sequence lifetimes ($\sim$19.8 Gyr for ϵ Eridani for instance) and thus slower temporal luminosity evolution across the main sequence bestows a significant advantage for evolution of life. The most optimal scenario is for initially warm planets. Terrestrial planets are believed to have been formed hot from accretion, and with an initially molten surface before their earliest atmospheres cooled and condensed. Thus, even though stellar luminosity increases in time, terrestrial planets likely begin their earliest histories in a hot state, and could then access a wider temperate zone, and undergo waterbelt states upon first cooling (Figure 4). Still, a waterbelt state may be a low-probability occurrence due to the narrow range of allowable stellar fluxes. Alternatively, waterbelt states could also occur if a planet formed with a larger primordial CO_2 inventory than assumed here, which is then drawn down over time by weathering processes, allowing the planet to cool (Abbot et al. 2011).

The maximum time spent in the habitable zone is $\sim$2.2, $\sim$2.4, and $\sim$4.7 Gyr for F-, G-, and K-dwarf planets respectively, possible only for warm start scenarios. Note that life has existed on Earth for at least 3.8 Gyr (Nisbet & Sleep 2001), significantly longer than the 2.4 Gyr lifetime noted here for a G-dwarf star. Long-lived habitable conditions for Earth are most likely due to a stronger CO_2 greenhouse early in Earth's history. See Section 4 for more discussion.

Table 3
Coefficients a, b, and c to be Used in Equation (1) to Calculate Circumstellar Climates Zones in Units of Relative Stellar Flux for Rapidly Rotating Earth-like Planets

Differentiations of Circumstellar Climate	a	b	c
Water Loss 1 Gyr ($T_s = 355$ K)[a]	1.19645	1.39815×10^{-4}	3.12706×10^{-8}
Temperate to Moist Greenhouse Transition	1.11892	8.48102×10^{-5}	3.89303×10^{-8}
Present Day Earth Conditions ($T_s = 289$ K)[b]	1.00014	6.81156×10^{-5}	2.12922×10^{-8}
Biological Heat Stress ($T_s = 300$ K)	1.06666	8.43240×10^{-5}	2.61308×10^{-8}
Temperate to Waterbelt Transition[b]	0.96011	5.54441×10^{-5}	7.18032×10^{-9}
Waterbelt to Snowball Transition[b]	0.92515	7.27318×10^{-5}	9.82310×10^{-10}
Snowball to Temperate Transition[c]	1.05521	1.07307×10^{-4}	-1.14135×10^{-8}

Notes. These parameterizations were fit to our model calculations. Valid for stars with 4900 K $\geqslant T_{\rm eff} \geqslant$ 6600 K.
[a] The water loss limit is the nominal inner edge of the habitable zone.
[b] Only accessible from warm start conditions.
[c] Only realizable from cold start conditions.
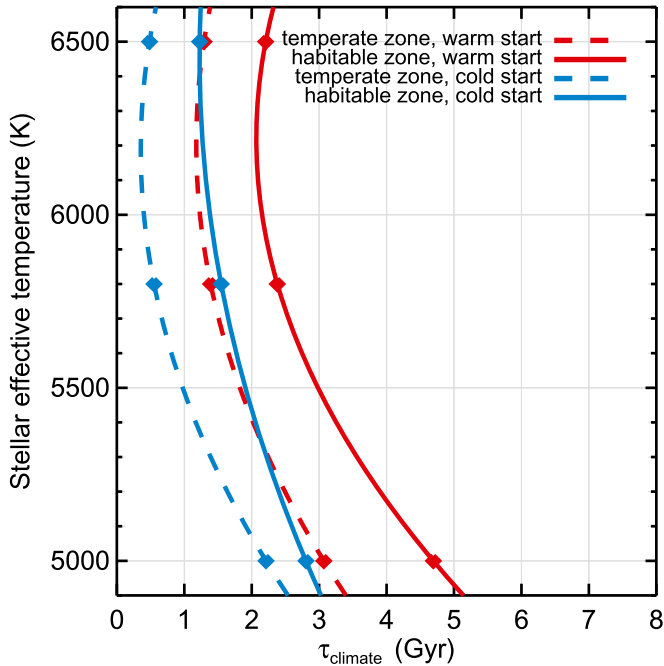
Figure 5. The lifetime of habitable (solid lines) and temperate (dashed lines) climate zones driven by main sequence brightening, for warm (red) and cold (blue) initial conditions respectively, as a function of the stellar effective temperature. These values represent the maximum possible time for these phases of climates to exist, without invoking a draw-down of CO_2 to stabilize climate against continued warming.

Cold start cases apply to initially frozen worlds subject to increased stellar fluxes whether by stellar evolution, or possibly planetary migration. For cold initial conditions, temperate climate states around F- and G-dwarf stars may last only $\sim$500 Myr if a draw-down of CO_2 is not invoked to mitigate warming. Interestingly, the habitable and temperate climate zone lifetimes are only about $\sim$10%–20% shorter for F-dwarf planets compared to G-dwarf planets, despite the F-dwarf having a total main sequence lifetime that is $\sim$40% shorter (6.4 Gyr versus 10.9 Gyr). Temperate Earth-like planets around F-dwarf stars benefit from their bluer stellar spectra, which is more effectively scattered and less readily absorbed by the near-IR water vapor bands, thus allowing for a temperate climate zone that exists under a wider range of relative stellar fluxes (Figures 2 and 4). Thus we should not ignore habitable zone planets around F-dwarf stars, due to their muted climate sensitivity.

4. Discussion

In this study we have fixed CO_2 at present day values; thus Figures 2 and 4 illustrate a relative range of habitable climates for a single choice for non-condensable greenhouse species. Couched in these terms, the habitable zone appears quite narrow for both warm and cold start scenarios. The wide range of stellar fluxes possible for the conventional habitable zone, as described in Kopparapu et al. (2013), is reliant on the strong greenhouse effect from multi-bar CO_2 atmospheres to set the outer edge of the habitable zone. It is conventionally thought that CO_2 can change on many planets and provide a stabilizing feedback to the climate system through the temperature-dependent action of the carbon/silicate cycle. If the temperature increases for some reason, weathering rates will increase, leading to removal of CO_2 from the atmosphere/ocean system and sequestration into sea floor carbonates such as limestone, which cools the planet by weakening the total greenhouse effect. Subduction of carbonate-rich sea floor on planets with plate tectonics, and subsequent volcanic outgassing, recycles the sea floor carbonates and supplies CO_2 to the atmosphere to balance the loss from weathering over geologically-long periods of time. Of course, silicate weathering requires the presence of continents and plate tectonics, both of which are uncertain.

However, if a planet has weak volcanic outgassing, perhaps in tandem with high rates of formation of seafloor carbonates, a cold planet may not be able accumulate sufficient CO_2 to deglaciate the planet independently of the stellar flux. Mars, for instance, currently resides within the habitable zone of Kopparapu et al. (2013), but it was unable to retain sufficient CO_2 to escape from its present frozen state. Kadoya & Tajika (2015) and Haqq-Misra et al. (2016) argue for Earth that if the paleo-CO_2 outgassing rates were less than on Earth presently, carbon/silicate cycles may not have been able to prevent a snowball glaciation for most of Earth's history. Furthermore, planets entering a snowball phase may oscillate between frozen and thawed states, with a frequency dependent on the rate of outgassing (Tajika 2007; Mills et al. 2011; Driscoll & Bercovici 2013; Haqq-Misra et al. 2016). Note that while the early Earth was indeed habitable for nearly its entire existence, implying higher CO_2 outgassing rates in the distant past to sustain a warm climate, there is geological evidence for periodic snowball glaciations up through the Neoproterozoic period, with the last being $\sim$635 Myr ago, when the solar constant was at $\sim$94% of its present day value (Kirschvink et al. 2000; Pierrehumbert et al. 2011). Interestingly, while
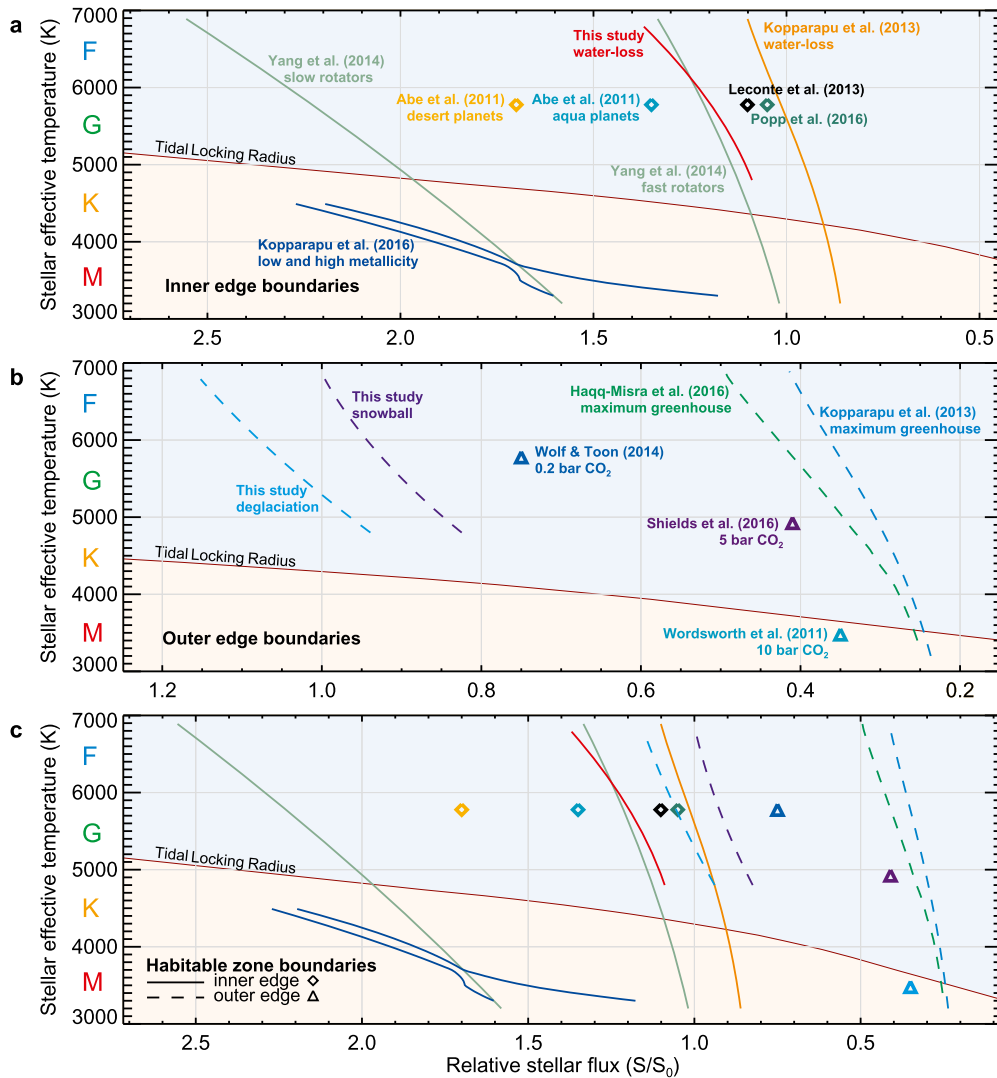
Figure 6. Constraints on the inner edge (a), outer edge (b), and total habitable zone (c) determined from recent modeling studies. In all panels, tidally locked planets reside in the light yellow shaded region while planets in the blue shaded region can rotate rapidly. Solid lines and diamonds are used to mark constraints on the inner edge of the habitable zone. Dashed lines and triangles are used to mark constraints on the outer edge of the habitable zone.

simple life emerged billions of years earlier, complex life did not emerge until the quasi-periodic snowball events ceased (Hoffman et al. 1998). While here we emphasize CO_2 and carbon/silicate cycles, there could be numerous other gases and particles in planetary atmospheres that could impact their climate that we have not considered, including N_2, H_2, CH_4, organic hazes, various sulfur compounds, and a host of others.

In Figure 6 we summarize habitable zone calculations published to date using 3D climate models of Earth-like planets, along with the widely used values of Kopparapu et al. (2013, 2014) that are based on 1D radiative-convective model calculations. Figure 6(a) shows constraints on the inner edge of the habitable zone derived from climate models with solid lines and diamonds. In theory, the inner edge of the habitable zone for a water-rich planet should not involve high levels of CO_2. As the climate warms, enhanced silicate weathering should draw down CO_2 to relatively low levels. Each simulation shown assumes a CO_2 mixing ratio equal to the modern Earth, along with 1 bar N_2 as the background gas. Numerous studies have calculated the inner edge of the habitable zone for Earth around the Sun ($T_{eff} = 5778$ K) using nationally supported 3D climate system models (Abe et al. 2011; Leconte et al. 2013;

Wolf & Toon 2014b, 2015; Yang et al. 2014; Popp et al. 2016). The models vary in the location of the inner edge of the habitable zone by $\sim 15\%$ (S/S_0). The models also differ in the predicted end state of the atmosphere. Leconte et al. (2013), using the LMD generic climate model, predict Earth will enter a runaway greenhouse and no moist greenhouse state is possible. On the contrary, both CAM (Wolf & Toon 2015) and ECHAM (Popp et al. 2016) models predict that a climatologically stable moist greenhouse state with significant water loss marks the inner edge of the habitable zone for Earth. Note that the results from this study, using a modified version of CAM4, appear quite similar to those of Yang et al. (2014), who used CAM3 (marked "fast" on Figure 6). However, the similarity between the two results is somewhat deceiving. Yang et al. (2014) derived the inner edge of the habitable zone at a point where the model becomes numerically unstable ($T_s \sim 310$ K). Here, numerical improvements to the convection scheme allow us to simulate much hotter temperatures, and define a true inner edge of the habitable zone by water loss from moist greenhouse atmospheres. Note also that the position of the inner edge determined by Yang et al. (2014) and Wolf & Toon (2015) is

also affected by differing properties of the radiative transfer model used (see Yang et al. 2016).

In all panels of Figure 6, light yellow and light blue shaded regions indicate regions in space that are inside and outside of the tidal locking radius respectively, following Edson et al. (2011) and Haqq-Misra & Kopparapu (2015). Tidal locking is expected to be most important for planets toward the inner edge of the habitable zone around low mass stars. Planets located within the tidal locking radius are strongly influenced by the host star gravity, and should exist in synchronous or resonant orbital–rotational configurations. However, tidal spin down may also be dependent upon atmospheric thickness and thermal tides (Leconte et al. 2015). Planets located in the blue region are unconstrained and can rotate rapidly as do Earth and Mars. There is a large difference between constraints for the inner edge of the habitable zone for rapidly rotating planets (Leconte et al. 2013; Yang et al. 2014; Godolt et al. 2015; Wolf & Toon 2015) and tidally locked planets, which tend to be more slowly rotating (Yang et al. 2014; Kopparapu et al. 2016). As first described by Yang et al. (2013), strong convection at the substellar point of slow rotators can create thick clouds that substantially raise the planet's albedo, thus allowing liquid surface water to exist under large stellar fluxes. Shown here are calculations from Yang et al. (2014) using CAM3 which assumed a fixed orbital–rotational period of 60 Earth days (marked "slow" on Figure 6(a)). However, in reality the orbital–rotation period and the stellar flux received by a tidally locked planet are dependent on the mass and luminosity of the stars, and should vary between ∼10 and 65 days for planets near the inner edge of the habitable zone around late-K and early-M stars. A subsequent revision of the inner edge of the habitable zone for these slow rotators was published by Kopparapu et al. (2016) using CAM4 and self-consistent orbital periods for both high and low metallicity stars. Changing the planetary rotation rate self-consistently has important consequences for atmospheric dynamics, cloud fields, and ultimately the global mean albedo and climate. Seamlessly connecting the habitable zones for rapid and slow rotators is not trivial. Near $T_{eff} \sim 4500$ K, the inner edge of the habitable zone for rapid rotators approaches the tidal locking radius. Here one may find a transition region between the fast and slow rotator limits, dependent upon planet–star tidal interactions and the precise rotation rate of the planet in question. It is clear from Figure 6(a) that the evolution of climate may critically depend on the evolution of the planetary rotation rate due to tidal interactions with the host star and also moons.

In Figure 6(b) we summarize constraints for the outer edge of the habitable zone and for habitable climates at low stellar fluxes and high-CO_2, with dashed lines and triangles. We include our estimates for the outer edge of the habitable zone based on snowball glaciation and stellar driven deglaciation limits for an Earth-like planet with modern CO_2. Note that in Figure 6(b) the "snowball" limit marks the transition between habitable and globally ice covered states due to decreasing stellar insolation (see also Figure 4(a)). The "deglaciation" limit marks the transition between globally ice covered and habitable states triggered by increasing stellar insolation (see also Figure 4(b)). Kasting et al. (1993) first postulated the so-called maximum CO_2 greenhouse limit for the outer edge of the habitable zone using a 1D radiative convective model. This limit has recently been revised for initially warm (Kopparapu

et al. 2013) and initially ice covered planets (Haqq-Misra et al. 2016), using a similar methodology with a 1D model. To date, no 3D simulations have calculated the maximum CO_2 greenhouse limit. However, several 3D studies have explored paleo-Earth, paleo-Mars, and high-CO_2 exoplanet scenarios, which may serve as useful steps toward determining the outer edge of the habitable zone around different stars (Wordsworth et al. 2011, 2013; Forget et al. 2013; Urata & Toon 2013; Wolf & Toon 2014a; Shields et al. 2016). Several of these data points are included in Figure 6(b) along with the CO_2 burden required to yield a habitable climate. More work is needed to define the maximum-CO_2 greenhouse for terrestrial planets using 3D models. Finally, Figure 6(c) combines habitability constraints from Figures 6(a) and (b) onto the same plot. It is clear that, without the ability to regulate CO_2 or other greenhouse gases, the habitable zone for rapidly rotating planets is quite narrow. Still, the effect of slowing rotation has an equally large effect in widening the total habitable zone. Information regarding planetary rotation rate, CO_2 cycling, and the ability of a planet to retain its atmosphere against escape are equally as important for determining habitability, as is the incident stellar flux.

5. Conclusions

In this paper, we have used a 3D climate system model to explore the effect of changing stellar fluxes on climate for an Earth-like exoplanet around F-, G-, and early K-dwarf main sequence stars, assuming a fixed amount of CO_2. For these stars, the inner edge of the habitable zone lies beyond the tidal-locking radius, and thus planets are free to maintain a rapid rotation rate. Earth-like planets in the habitable zone are subject to four stable climate states (snowball, waterbelt, temperate, and moist greenhouse), each separated by sharp climatic transitions which are triggered by the changing thermodynamic partitioning of water in the climate system. Without allowing for the build up or removal of non-condensable greenhouse gas species such as CO_2, the range of relative stellar fluxes that permits temperate climates (i.e., $275 \leqslant T_s \leqslant 315$ K) is quite narrow: $\Delta S/S_0 \sim 0.06$–0.11 for initially frozen planets and $\Delta S/S_0 \sim 0.16$–0.20 for initially warm planets. The range of habitable climates becomes marginally wider if we generously allow both waterbelt and cooler moist greenhouse climates ($T_s \leqslant 330$ K) to be included as habitable worlds: $\Delta S/S_0 \sim 0.14$–0.19 for initially cold planets and $\Delta S/S_0 \sim 0.24$–0.34 for initially warm planets. For cold initial conditions, planets around K-dwarf stars have the widest habitable zones due to deglaciation of sea ice at lower stellar fluxes. For warm initial conditions, planets around F-dwarf stars have the widest habitable zones due primarily to a muted climate sensitivity across a broad temperate climate zone. These variations in the stellar flux represent only a small fraction of the total change in stellar flux that occurs over the host star's main sequence lifetime. Among our studied systems, the K-dwarf stars provide the longest lived habitable climates due to their lengthy main sequence lifetimes, and thus relatively slow rate of main sequence brightening.

The reader is also reminded that results presented in this work are derived from a single three-dimensional climate system model. Differences in radiative transfer, convection, clouds, ocean heat transport, sea ice, and other processes can vary across different 3D models, and can lead to significant differences in the resultant climates. Furthermore, we have only studied two parameters

(stellar flux and spectrum) in detail. The computational expense of modern climate models requires a focused approach to the study of parameter spaces relevant to habitable extrasolar planets. Lower dimensional models retain significant value by allowing multi-dimensional parameter sweeps with relative ease. The standard approximation taken here of the proverbial Earth-like exoplanet is now well worn. We hope these simulations mark an appropriate starting point for intercomparison among current climate models for Earth-like planets around various stars, before continuing toward habitable planets having more exotic characteristics. Model intercomparison is needed to constrain the origin of differences found in various simulations, some of which are noted in Figure 6. The differences might arise from different model parameterizations of radiative transfer, clouds, convection, large-scale dynamics, or some other process.

While much effort in the literature has been given to defining the effect of the stellar flux on habitable climates, it is clear that the geological and/or biological regulation of non-condensable greenhouse species is of equal or possibly greater importance to planetary habitability, by allowing the habitable zone to be extended much further away from the host star. Lastly, to complete our picture of the inner edge of the habitable zone, future work might focus on the 4500–5000 K effective temperature regime, where the inner edge of the habitable zone for rapid rotators approaches the tidal-locking radius.

References

Abbot, D. S., Voigt, A., & Koll, D. 2011, JGR, 116, D18103
Abe, Y., Abe-Ouchi, A., Sleep, N. H., & Zahnle, K. J. 2011, AsBio, 11, 443
Andrews, T., Gregory, J. M., Webb, M. J., & Taylor, K. E. 2012, GeoRL, 39, L09712
Boschi, R., Lucarini, V., & Pascale, S. 2013, Icar, 226, 1724
Brieglebb, B. P. 1992, JGR, 97, 7603
Budyko, M. I. 1969, Tell, 21, 611
Del Genio, A. D. 2016, arXiv:1603.07424
Driscoll, P., & Bercovici, D. 2013, Icar, 226, 1447
Dunkle, R. V., & Bevans, J. T. 1956, J. Meteorol., 13, 212
Edson, A., Lee, S., Bannon, P., et al. 2011, Icar, 212, 1
Flato, G., Marotzke, J., Abiodun, B., et al. 2013, in Climate Change 2013: The Physical Science Basis. Contribution of Working Group I to the Fifth Assessment Report of the Intergovernmental Panel on Climate Change 741, ed. T. Stocker et al. (Cambridge: Cambridge Univ. Press)
Forget, F., Wordsworth, R., Millour, E., et al. 2013, Icar, 222, 81
Gardner, J. P., Mather, J. C., Clampin, M., et al. 2006, SSRv, 123, 485
Godolt, M., Grenfell, J. L., Haman-Reinus, A., et al. 2015, P&SS, 111, 62
Guo, J., Zhang, F., Chen, X., & Han, Z. 2009, Ap&SS, 323, 367
Habets, G. M. H. J., & Heintze, J. R. W. 1981, A&AS, 46, 193
Hack, J. J. 1994, JGR, 99, 5551
Haqq-Misra, J., & Kopparapu, R. K. 2015, MNRAS, 446, 428
Haqq-Misra, J., Kopparapu, R. K., Batalha, N. E., et al. 2016, ApJ, 827, 120
Hart, M. H. 1979, Icar, 37, 351
Hoffman, P. F., Kaufman, A. J., Kalverson, G. P., & Schrag, D. P. 1998, Sci, 281, 1342
Iben, I. 1967, ARA&A, 5, 571
Joshi, M. M., & Haberle, R. M. 2012, AsBio, 12, 3
Kadoya, S., & Tajika, E. 2015, ApJL, 815, L7
Kasting, J. F., Whitmire, D. P., & Reynolds, R. T. 1993, Icar, 101, 108
Kirschvink, J. L., Gaidos, E. J., Bertani, L. E., et al. 2000, PNAS, 97, 1400
Kopparapu, R. K., Ramirez, R., Kasting, J. F., et al. 2013, ApJ, 765, 131
Kopparapu, R. K., Ramirez, R. M., Kotte, J. S., et al. 2014, ApJL, 787, L29
Kopparapu, R. K., Wolf, E. T., Haqq-Misra, J., et al. 2016, ApJ, 819, 84
Leconte, J., Forget, F., Charnay, B., et al. 2013, Natur, 504, 268
Leconte, J., Wu, H., Menou, K., & Murray, N. 2015, Sci, 347, 632
Lucarini, V., Fraedrich, K., & Lunkeit, F. 2010, QJRMS, 136, 2
Mills, B., Watson, A. J., Goldblatt, C., et al. 2011, NatGe, 4, 861
Neale, R. B., Richter, J. H., Conley, A. J., et al. 2010, TN-486/TN-486+STR, http://www.cesm.ucar.edu/models/ccsm4.0/cam/docs/description/cam4_desc.pdf
Nisbet, E. G., & Sleep, N. H. 2001, Natur, 409, 1083
Pickles, A. J. 1998, PASP, 110, 863
Pierrehumbert, R. T., Abbot, D. S., Voigt, A., & Koll, D. 2011, AREPS, 39, 417
Popp, M., Schmidt, H., & Marotzke, J. 2016, NatCo, 7, 10627
Poulsen, C. J., Pierrehumbert, R. T., & Jacob, R. L. 2001, GeoRL, 28, 1575
Ramanathan, V., & Downey, P. 1986, JGR, 91, 8649
Rasch, P. J., & Kristjánsson, J. E. 1998, JCli, 11, 1587
Ricker, G. R., Winn, J. N., Vanderspek, R., et al. 2014, Proc. SPIE, 9143, 914320
Rugheimer, S., Segura, A., Kaltenegger, L., & Sasselov, D. 2015, ApJ, 806, 137
Rushby, A. J., Claire, M. W., Osborn, H., & Watson, A. J. 2013, AsBio, 13, 833
Segura, A., Krelove, K., Kasting, J. F., et al. 2003, AsBio, 3, 689
Selsis, F., Kasting, J. F., Levrard, B., et al. 2007, A&A, 476, 1373
Sherwood, S. C., & Huber, M. 2010, PNAS, 107, 9552
Shields, A. L., Barnes, R., Agol, E., et al. 2016, AsBio, 16, 443
Shields, A. L., Bitz, C. M., Meadows, V. S., et al. 2014, ApJL, 785, L9
Shields, A. L., Meadows, V. S., Bitz, C. M., et al. 2013, AsBio, 13, 715
Tajika, E. 2007, EP&S, 59, 293
Urata, R. A., & Toon, O. B. 2013, Icar, 226, 229
Way, M. J., Del Genio, A. D., Kiang, N. Y., et al. 2016, GeoRL, 43, 8376
Wolf, E. T., & Toon, O. B. 2013, AsBio, 13, 1
Wolf, E. T., & Toon, O. B. 2014a, GeoRL, 41, 167
Wolf, E. T., & Toon, O. B. 2014b, AsBio, 14, 241
Wolf, E. T., & Toon, O. B. 2015, JGRD, 120, 5775
Wordsworth, R., Forget, F., Millour, E., et al. 2013, Icar, 222, 1
Wordsworth, R. D., Forget, F., Selsis, F., et al. 2011, ApJL, 733, L48
Yang, J., Boue, G., Fabrycky, D. C., & Abbot, D. S. 2014, ApJL, 787, L2
Yang, J., Cowan, N., & Abbot, D. S. 2013, ApJL, 771, L45
Yang, J., Leconte, J., Wolf, E. T., et al. 2016, ApJ, 826, 222
Zhang, G. J., & McFarlane, N. A. 1995, AtO, 33, 407
Zsom, A., Seager, S., de Wit, J., & Stamenković, V. 2013, ApJ, 778, 109